

1 **Distribution of Earth's radiation belts protons over the drift**
2 **frequency of particles**

3 **Alexander S. Kovtyukh**

4 Skobeltsyn Institute of Nuclear Physics, Moscow State University, Moscow, 119234, Russia

5 Correspondence: Alexander S. Kovtyukh (kovtyukhas@mail.ru)

6 **Abstract.** On the data for the proton fluxes of the Earth's radiation belts (ERB) with energy
7 ranging from 0.2 to 100 MeV on the drift L shells ranging from 1 to 8, the quasi-stationary
8 distributions over the drift frequency f_d of protons around the Earth are constructed. For this
9 purpose, direct measurements of proton fluxes of the ERB in the period 1961–2017 near the
10 geomagnetic equator were employed. The main physical processes in the ERB manifested more
11 clearly in these distributions, and for protons with $f_d > 0.5$ mHz at $L > 3$ their distributions in the
12 space $\{f_d, L\}$ have a more regular shape than in the space $\{E, L\}$. It has been found also that the
13 quantity of the ERB protons with $f_d \sim 1\text{--}10$ mHz at $L \sim 2$ does not decrease, as for protons with
14 $E > 10\text{--}20$ MeV (with $f_d > 10$ mHz), but increases with an increase in solar activity. This means
15 that the balance of radial transport and losses of the ERB low-energy protons at $L \sim 2$ is
16 disrupted in advantage of transport for these protons: the effect of an increase in the radial
17 diffusion rates with increasing solar activity, overpowers the effect of an increase in the density
18 of the dissipative medium.

19
20
21 **Keywords.** Magnetospheric physics (energetic particles, trapped). Radiation belts.

22

23 **1 Introduction**

24 The Earth's radiation belts (ERB) consist mainly of charged particles with energy from $E \sim 100$
25 keV to several hundreds of megaelectronvolt (MeV). In the field of the geomagnetic trap, each
26 particles of the ERB with energy E and equatorial pitch-angle α_0 (α is the angle between the local
27 vector of the magnetic field and the vector of a particle velocity) makes three periodic movements:
28 Larmor rotation, oscillations along the magnetic field line, and drift around the Earth (Alfvén and
29 Fälthammar, 1963; Northrop, 1963).

30 Three adiabatic invariants (μ , K , Φ) correspond to these periodic motions of trapped particles,
31 as well as three periods of time or three frequencies: a cyclotron frequency f_c , a frequency of
32 particle oscillations along the magnetic field line f_b , and a drift frequency of particles around the
33 Earth f_d . For the near-equatorial ERB protons, we have: $f_c \sim 1\text{--}500$ Hz, $f_b \sim 0.02\text{--}2$ Hz and $f_d \sim 0.1\text{--}$
34 20 mHz. The frequency f_c increases by tens to hundreds of times with the distance of the particle
35 from the plane of the geomagnetic equator (in proportion to the local induction of the magnetic
36 field), and the frequency f_b decreases by almost 2 times with increasing amplitude of particles
37 oscillation.

38 The number of particles with a given frequency f_c decreases rapidly with an increase of L , and
39 refers to higher and higher geomagnetic latitudes. For each given frequency f_b , particles become
40 more and more energetic with an increase of L ($E \propto L^2$) and their number becomes smaller.

41 Compared to the frequencies f_c and f_b , the drift frequency f_d for one particle species has a much
42 narrower range of values; it does not depend on the mass of the particles and it very weakly
43 depends on the amplitude of their oscillations (vary within $\sim 20\%$); in this case, on each L -shell
44 there are a significant number of particles corresponding to a certain value of f_d .

45 Therefore, it can be expected that the distributions of the ERB particles in the space $\{f_d, L\}$ will
46 have a more regular shape than in the space $\{E, L\}$, and the main physical processes in these belts
47 will manifest themselves more clearly in these distributions. Furthermore, it can also be expected
48 that on these more ordered background more fine features can be revealed that would not appear in
49 the space $\{E, L\}$.

50 Despite the importance of the drift frequency f_d for the mechanisms of the ERB formation,
51 reliable and sufficiently complete distributions of particles in the ERBs (over the frequency f_d)
52 have not been presented nor analyzed; indeed, this is the first time.

53 The analysis presented in this paper is limited to the protons of the ERB during magnetically
54 quiet periods of observations ($Kp < 2$), when the proton fluxes and their spatial-energy
55 distributions were quasi-stationary. In the following sections, the distributions of the ERB protons
56 over their drift frequency f_d are constructed from experimental data (Sect. 2), and analyzed (Sect.
57 3). The main conclusions of this work are given in Sect. 4.

58 **2 Constructing the distributions of the ERB protons over their drift frequency**

59 The problem of methodical differences in measurements of the fluxes of protons of the radiation
60 belts on different satellites was one of the main ones in this work. From the published
61 experimental data, one selected those that are in good agreement with each other and exclude from
62 consideration all unreliable measurement results (with admixture of electrons and various ionic
63 components of the ERB to the protons). Then, these reliable experimental results for proton fluxes
64 and their anisotropy near the equatorial plane were represent in the space $\{E, L\}$; this space is very
65 efficient with respect to organizing experimental data obtained in different ranges of E and L .

66 In such representation of experimental data, there is no need for interpolation and extrapolation
67 of fluxes on the energy (in other representations, such necessity arises due to differences in

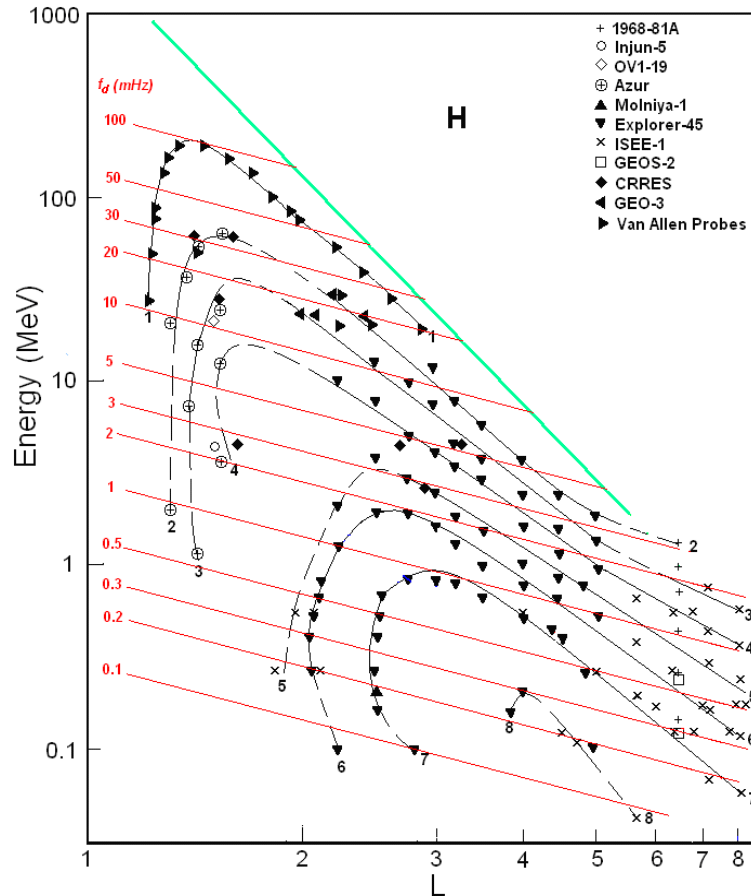
68 channel widths and their positions on the energy scale for instruments installed on different
 69 satellites). In addition, with such a representation, in one figure, the data of various experiments, it
 70 is possible to construct the isolines of fluxes (and anisotropy of fluxes); these isolines cannot
 71 intersect with each other and, thus, allow to exclude a data that sharply fall out of the general
 72 picture (for more details see in Kovtyukh, 2020).

73 2.1 Spatial-energy distributions of the ERB protons near the equatorial plane

74 To construct the distributions of the ERB particles over the drift frequency, it is necessary to have
 75 reliable distributions of the differential fluxes of the ERB protons in the space $\{E, L\}$, where E is
 76 the kinetic energy of protons and L is the drift shell parameter.

77 From the data of averaged satellite measurements of the differential fluxes of protons with an
 78 equatorial pitch-angle $\alpha_0 \approx 90^\circ$, aforementioned distributions are constructed in (Kovtyukh, 2020)
 79 during quiet periods ($K_p < 2$) near solar activity maximum in 20th (1968–1971), 22th (1990–
 80 1991), 23th (2000), and 24th (2012–2017) solar cycles. Such distributions, separately for minima
 81 and maxima of the 11-year solar activity cycles, are constructed from satellite data also for other
 82 ionic components of the ERB (near the equatorial plane), but the most reliable and detailed picture
 83 was obtained in for protons (see Kovtyukh, 2020).

84 In Fig. 1 one of these distributions is reproduced for periods near solar maxima (on the data
 85 from 1968 to 2017); here, data of different satellites are associated with different symbols. The
 86 numbers on the curves (isolines) refers to the values of the decimal logarithms of the differential
 87 fluxes J ($\text{cm}^2 \text{ s sr MeV}^{-1}$) of protons (with equatorial pitch-angle $\alpha_0 \approx 90^\circ$). The red lines
 88 correspond to the dependences $f_d(\text{mHz}) = 0.379 \cdot L \cdot E(\text{MeV})$ for the drift frequency of the near-
 89 equatorial protons in the dipole approximation of the geomagnetic field.



91 **Figure 1.** Distribution of the differential fluxes J in the space $\{E, L\}$ for protons with $\alpha_0 \approx 90^\circ$ near maxima of the
 92 solar activity (from Kovtyukh, 2020). Data of satellites are associated with different symbols. The numbers on the
 93 curves refers to the values of the decimal logarithms of J . Fluxes is given in units of $(\text{cm}^2 \text{ s sr MeV})^{-1}$. The red lines
 94 corresponds to the drift frequency f_d (mHz). The green line corresponds to the maximum energy of the trapped protons.

95 During quiet periods considered in this work, the geomagnetic field at $L < 5-5.5$ is close to the
 96 dipole configuration and $L \approx L^*$. At large L , the magnetic field differs from the dipole one even in
 97 quiet periods; it leads to the flattening of the isolines of the proton fluxes at $L > 5$ in Fig. 1.

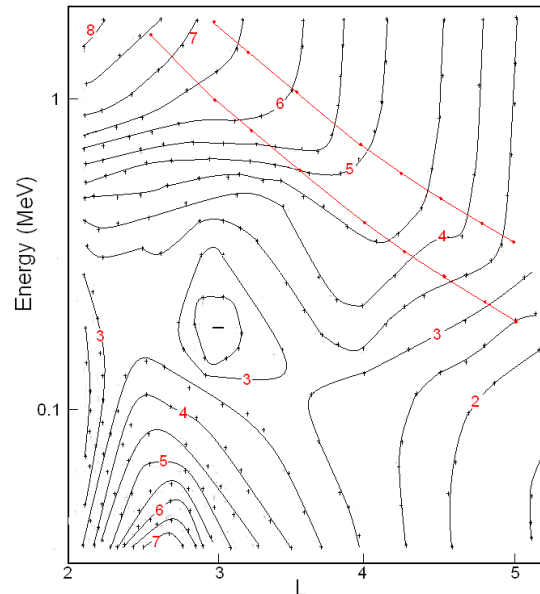
98 Only protons with energies less than some maximum values, determined by the Alfvén's
 99 criterion: $\rho_c(L, E) \ll \rho_B(L)$, where ρ_c is the gyroradius of protons, and ρ_B is the radius of curvature
 100 of the magnetic field (near the equatorial plane) can be trapped on the drift shells. According to
 101 this criterion and to the theory of stochastic motion of particles, the geomagnetic trap in the dipolar
 102 region can capture and durably hold only protons with E (MeV) $< 2000 \cdot L^{-4}$ (Ilyin et al., 1984). The
 103 green line in Fig. 1 represents this boundary.

104 The distribution of the ERB proton fluxes shown in Fig. 1, refers to the years of the solar
 105 maximum, but the solar-cyclic variations in the ERB proton fluxes are small and localized at $L <$
 106 2.5 (see Kovtyukh, 2020).

107 2.2 Spatial-energy distributions of the ERB protons outside the equatorial plane

108 The quasi-stationary fluxes J of the ERB particles with given energy and local pitch-angle α
 109 decrease usually when the point of observation is shifted from the equatorial plane to higher
 110 latitudes along a certain magnetic field line. In the inner regions of the ERB, on $L < 5$, an angular
 111 distributions of protons have usually a maximum at the local pitch-angle $\alpha = 90^\circ$. In wide interval
 112 near this maximum these distributions are well described by the function
 113 $J(\alpha, B/B_0) \propto (B/B_0)^{-A/2} \sin^A \alpha$ (Parker, 1957), where A is the index of an anisotropy of a
 114 fluxes, B is the induction of a magnetic field at the point of measurements of these fluxes and B_0 is
 115 induction of a magnetic field at the equatorial plane on the same magnetic line.

116 The empirical model of an anisotropy $A(E, L)$ for the proton fluxes with $E \sim 0.1-2$ MeV on $L \sim$
 117 $2-5$ near the equatorial plane for the quasi-stationary ERB (for quiet periods with $\text{Kp} < 2$) is
 118 presented in Fig. 2. The anisotropy index A of these fluxes is shown in Fig. 2, in the space $\{E, L\}$,
 119 in the form of isolines with the same values A from 1.5 to 8.0 and with a step $\Delta A = 0.5$. The integer
 120 values of this index are plotted on the corresponding isolines as red numbers.



122 **Figure 2.** Empirical model of the anisotropy index $A(E, L)$ of the ERB proton fluxes averaged on the data of the
 123 satellites obtained near the plane of the geomagnetic equator. Values of A are given on isolines of the anisotropy: $A =$
 124 1.5–8.5 with the step $\Delta A = 0.5$.

125 When constructing this model, we consider and analyze the data of the following satellites:
 126 Explorer-12 (Hoffman and Bracken, 1965), Explorer-14 (Davis, 1965), Explorer-26 (Søraas and
 127 Davis, 1968), OV1-14 and OV1-19 (Fennell et al., 1974), Explorer-45 (Williams and Lyons, 1974;
 128 Fritz and Spjeldvik, 1981; Garcia and Spjeldvik, 1985), ISEE-1 (Garcia and Spjeldvik, 1985;
 129 Williams and Frank, 1984), SCATHA (Blake and Fennell, 1981), Van Allen Probes (Shi et al.,
 130 2016), and other satellites. These data were obtained in 1961-2015.

131 Fig. 2 shows that for rather high energy (> 1 MeV) the anisotropy of a proton fluxes
 132 monotonically increases with decreasing L (from $A \sim 3.5$ to $A \sim 8.0$). For $E > 0.3$ MeV on $L < 3$
 133 anisotropy is monotonically increases with increasing energy, but for $E > 0.5$ MeV on $L > 3$ it is
 134 almost energy-independent.

135 Some small irregularities of the isolines in Fig. 2 are due to the fact that experimental data were
 136 used for constructing this figure were obtained in different years, with different instruments, and
 137 during different intensity of the solar activity. At the same time, Fig. 2 demonstrates the important
 138 regularities of the pitch-angle distributions of the quasi-stationary ERB proton fluxes.

139 In the region $\{E > 0.5$ MeV, $L > 3\}$ the isolines of the anisotropy index are almost parallel to
 140 each other and to the energy axis. This adiabatic regularity refers to protons belonging to the
 141 power-law tail of their energy spectra, the exponent of which practically does not change when L
 142 changes (at $L > 3$). In Fig. 2, the red lines correspond to the lower boundary of the power-law tail
 143 of the ERB protons energy spectra: $E_b = (36 \pm 11) L^{-3}$ MeV (see Kovtyukh, 2001, 2020).

144 The pattern of $A(E, L)$ in the region on $L > 3$ at $E \sim 0.2$ – 0.5 MeV and the local minimum at $L \sim$
 145 3 ($E \sim 0.2$ MeV) are connected with local maximum in the quasi-stationary proton energy spectra
 146 of the ERB which corresponds to $E = (17 \pm 3) L^{-3}$ MeV (see Kovtyukh, 2001, 2020).

147 These regularities in the pattern of $A(E, L)$ are explained within the framework of the theory of
 148 radial transport (diffusion) of the ERB protons with conservation of the adiabatic invariants μ and
 149 K of their periodic motions (these issues were most fully considered in Kovtyukh, 1993).

150 Both the local maximum at $L \sim 2.5$ ($E < 0.1$ MeV) and the region of low anisotropy at $L \sim 2$ (E
 151 ~ 0.1 MeV) in Fig. 2, are related to the ionization losses of protons.

152 On the data of the satellites, the pitch-angle distributions of the ERB proton fluxes strongly
 153 depend on MLT at $L > 5$: the average index A values on the day side are larger than on the night
 154 side, and this dependence becomes more distinct with increasing energy (see, e.g., Shi et al., 2016).
 155 These results indicate that drift shells splitting (Roederer, 1970) play an important role in the
 156 formation of these distributions at $L > 5$. In the calculations performed here, it was assumed that
 157 near the equatorial plane the pitch-angle distributions of the ERB proton fluxes at $L > 6$, averaged
 158 over MLT, at $\alpha_0 \sim 90^\circ$ are nearly isotropic.

159 High anisotropy for the fluxes of protons at $E = 5$ – 50 MeV and a strong dependence $A(L)$ at the
 160 inner boundary of the inner belt ($L = 1.15$ – 1.40 , $B/B_0 = 1.0$ – 1.7) were obtained on the satellite
 161 DIAL (Fischer et al., 1977). According to these data, an anisotropy index increase from $A \sim 12$ at L
 162 $= 1.25$ to $A \sim 60$ at $L = 1.15$, and do not depends on L at $L = 1.25$ – 1.40 . These results are supported
 163 by the data of the satellite Resurs-01-N4 for the protons with $E = 12$ – 15 MeV which were obtained
 164 at $h \sim 800$ km (Leonov et al., 2005). They will be taken into account in our calculations.

165 The experimental results on the pitch-angle distributions of the ERB proton fluxes and their
 166 anisotropy indexes were discussed in detail in (Kovtyukh, 2018).

167 **2.3 Drift frequency distributions of the ERB protons**

168 Based on the results shown in Fig. 1 and 2, one can calculate the distributions of the ERB protons
 169 over the drift frequency f_d . In these calculations, the dipole model of the geomagnetic field was

170 used, according to which (see, e.g., Roederer, 1970) the point of the magnetic field line at a given
 171 L and a geomagnetic latitude λ is located from the center of the dipole at a distance

$$172 \quad R(L, \lambda) = R_E L \cos^2 \lambda,$$

173 where R_E is the Earth's radius, and the field induction at a given L changes with changing λ as

$$174 \quad B(L, \lambda) = \frac{\sqrt{4 - 3 \cos^2 \lambda}}{\cos^6 \lambda} B_0(L),$$

175 where $B_0(L) = 0.311 \text{ G} \times L^{-3}$.

176 It was also taken into account that the drift frequency f_d of the nonrelativistic particles depends
 177 essentially only on their kinetic energy E and on L . This value depends very slightly on the particle
 178 pitch-angle: with an increase in the geomagnetic latitude of the mirror point of the particle trajectory
 179 from 0 to 10° , it increases by only 1.5% and in the range from 0 to $20\text{--}30^\circ$ it increases by 5.8–12.5%.

180 The number of protons with energies from E to $E+dE$ per unit volume n is equal to the differential
 181 flux of these particles J (falling per unit time per unit area of the detector per unit solid angle), divided
 182 by the velocity v of these particles: $n = J/v$. For nonrelativistic protons with mass m , this velocity is
 183 $(2E/m)^{1/2}$.

184 Then in the near-equatorial region, between L and $L+dL$ and within geomagnetic latitudes from
 185 0 to $\pm\lambda_0$, the total number of nonrelativistic protons with mirror points within this region and with
 186 energy from E to $E+dE$, drifting on a given L with frequency $f_d(L, E)$ around the Earth, is

$$187 \quad \Delta N(L, f_d) = 2 \int_0^{\lambda_0} 2\pi R_E^2 L dL \frac{B_0(L)}{B(L, \lambda)} R_E L \cos \lambda \sqrt{4 - 3 \cos^2 \lambda} d\lambda \times$$

$$4\pi \int_{\alpha_{01}}^{\alpha_{02}} \frac{J(L, E(L, f_d)) dE}{\sqrt{2E(L, f_d)/m}} \sin^A \alpha_0 \cos \alpha_0 d\alpha_0,$$

188 where m is the rest mass of a proton, $J(L, E(L, f_d))$ is the differential fluxes and $E(L, f_d)$ is the
 189 protons energy. The first integral takes into account that the magnetic flux in the layer between
 190 shells L and $L+dL$ it conserved when latitude λ changes, i.e.

$$191 \quad 2\pi R_E L \cos \lambda R_E dL = 2\pi R_E L \frac{B_0(L)}{B(L, \lambda)} R_E dL.$$

192 As result of integrating the last expression over α_0 and replacing $\cos \lambda \equiv t$, we obtain:

$$193 \quad \Delta N(L, f_d) = 4\pi R_E^3 L^2 dL \frac{J(L, E(L, f_d)) dE}{\sqrt{2E(L, f_d)/m}} \times \frac{4\pi}{A+1} \times$$

$$\int_{\cos \lambda_0}^1 t^7 \left[\left(\frac{t^6}{\sqrt{4-3t^2}} \right)^{\frac{A+1}{2}} - (0.565)^{A+1} \right] dt$$

194 When integrating over equatorial pitch-angles α_0 , Liouville's theorem and the conservation of
 195 the first adiabatic invariant (μ) are taken into account: $\sin^2 \alpha_{01} = B_0(L)/B(L, \lambda_0)$ and $\sin^2 \alpha_{02} =$
 196 $B_0(L)/B(L, \lambda)$, where $B(L, 0) = B_0(L)$.

197 With an increase λ from 0 to $\lambda_0 = 30^\circ$, the value of the function $\sqrt{4-3t^2}$ increases from 1 to
 198 1.32, i.e. deviates from the average value (1.16) by only 16%. Most part of the ERB protons are

199 concentrated at these latitudes. Therefore, when calculating the last integral, we will assume that
 200 $\sqrt{4-3t^2} \approx 1.16$.

201 Then you can get the following expression:

$$202 \quad \Delta N(L, f_d) = k \frac{J(L, E(L, f_d))}{\sqrt{E(L, f_d)}} F(A) L^2 dL dE ,$$

203 where

$$204 \quad F(A) = \frac{1}{A+1} \left[\frac{(1.16)^{-(A+1)/2}}{3A+11} (1-0.21 \cdot 0.65^A) - 0.085(0.565)^{A+1} \right]$$

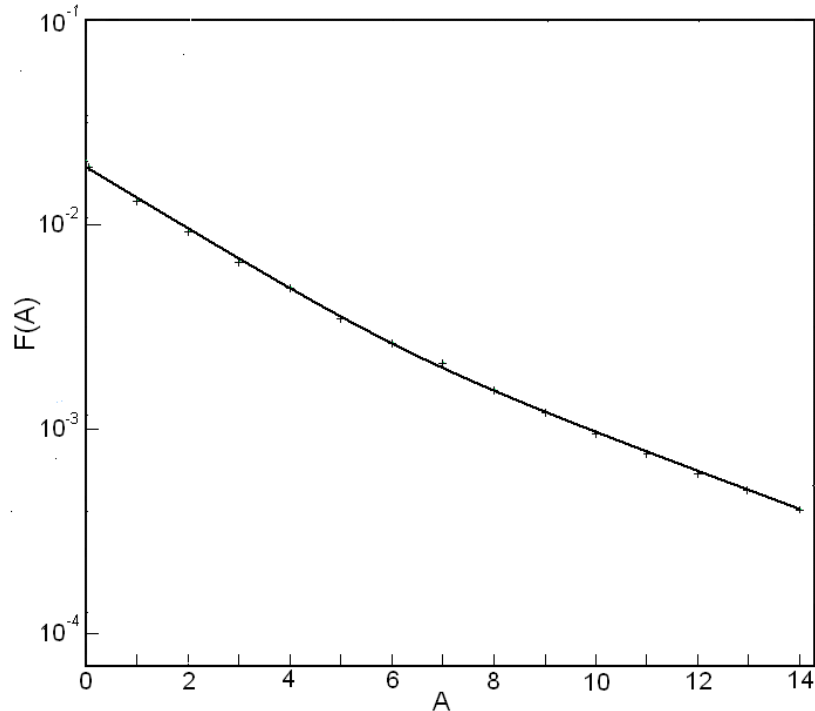
206 and

$$207 \quad k = (4\pi)^2 R_E^3 \sqrt{m/2} = 2.945 \cdot 10^{19} \text{ cm}^2 \text{ s sr MeV}^{1/2} .$$

208 When calculating the values of ΔN , we will take that $dL/L = dE/E = 0.1$. Finally, for the
 209 indicated ERB region near the equatorial plane, we obtain:

$$210 \quad \Delta N(L, f_d) = 2.945 \cdot 10^{17} J(L, E(L, f_d)) \sqrt{E(L, f_d)} F(A) L^3 , \quad (1)$$

211 where J , the differential fluxes of protons with equatorially pitch-angle $\alpha_0 \approx 90^\circ$, is given in units
 212 of $(\text{cm}^2 \text{ s sr MeV})^{-1}$, and the energy of protons E is given in MeV. The dependence $F(A)$ is shown
 213 in Fig. 3.

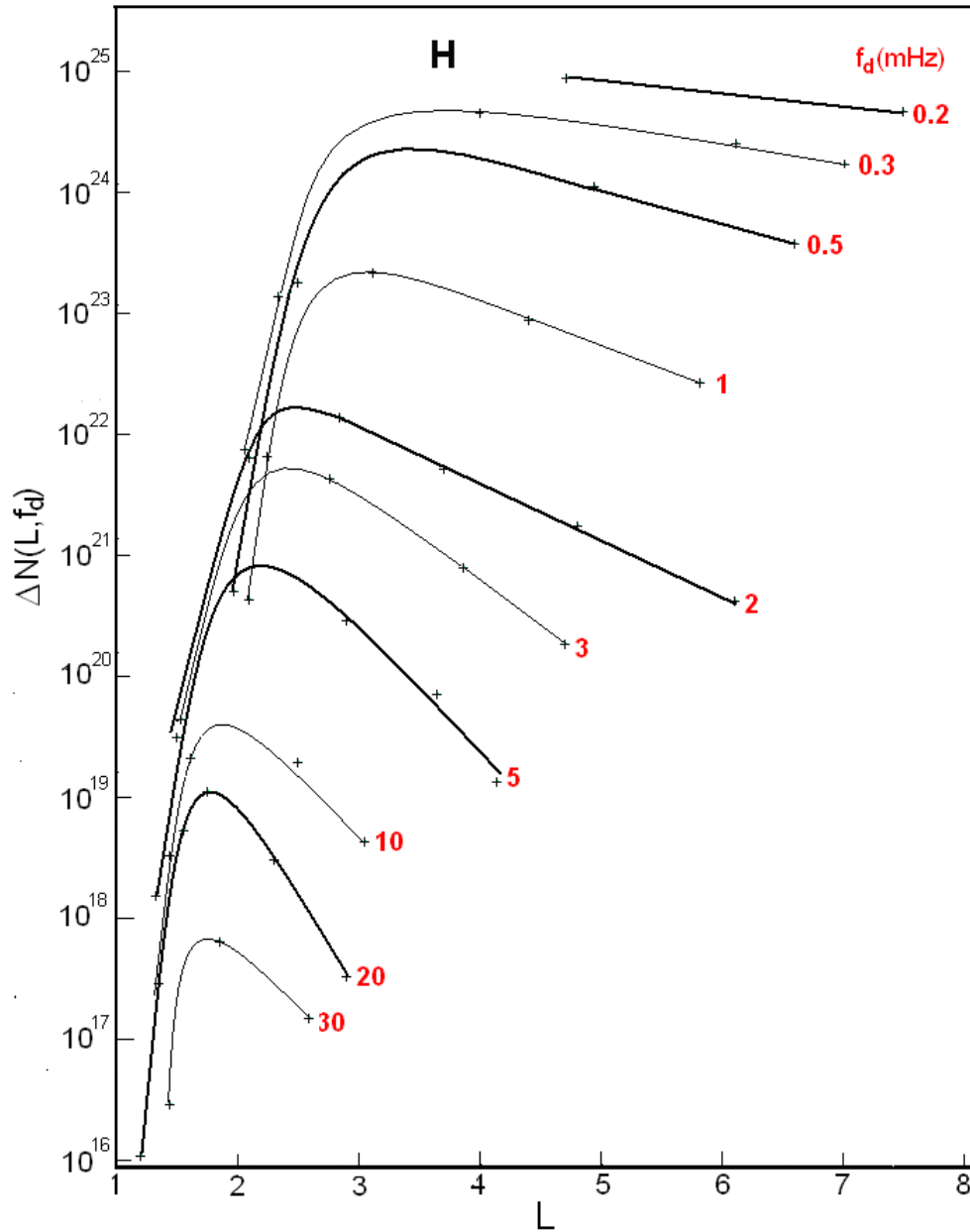


214

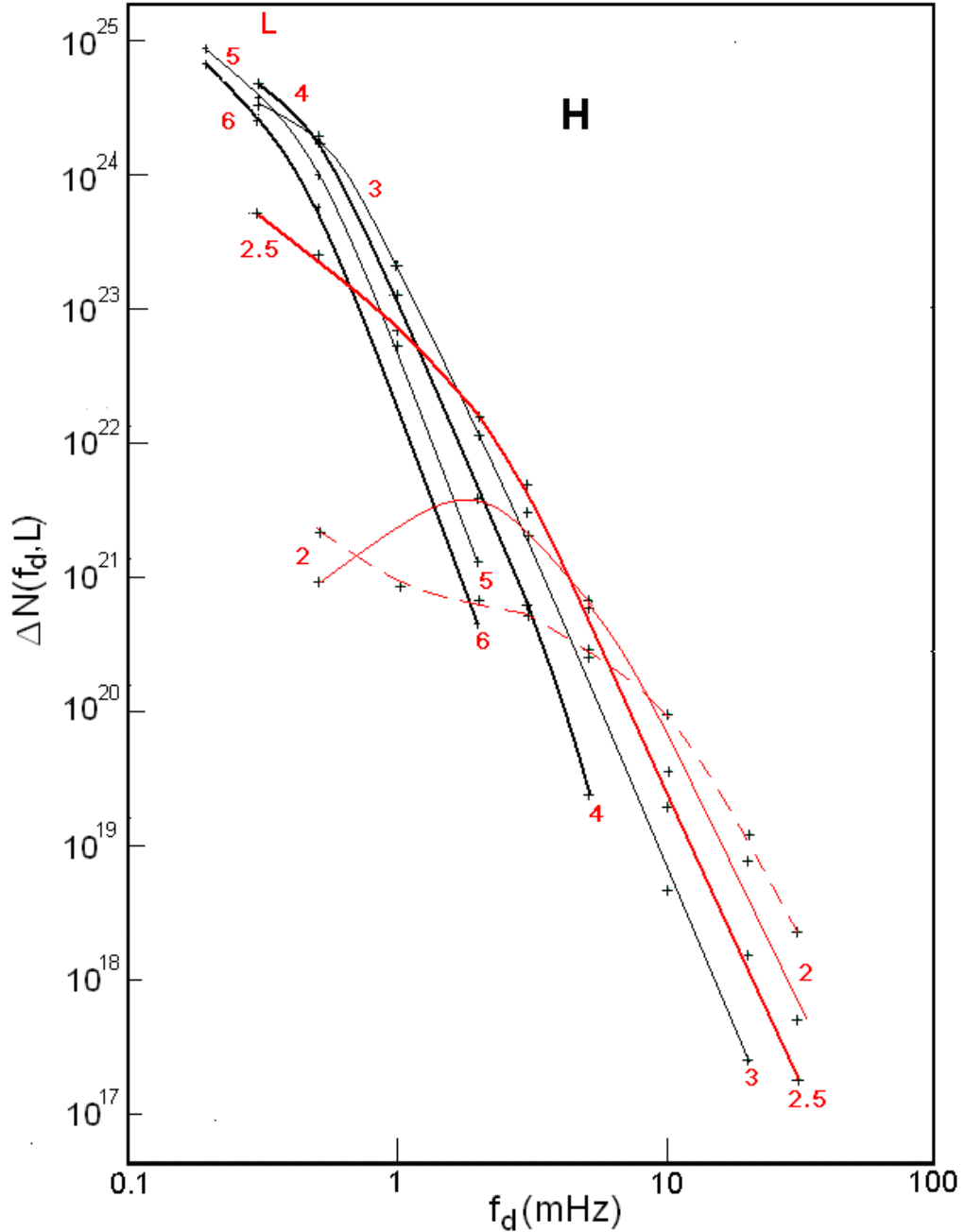
215 **Figure 3.** Dependence of the factor $F(A)$ in formula (1) on the anisotropy index A of the proton fluxes.

216 For protons of the ERB, the radial profiles $\Delta N(L, f_d)$ for $f_d = 0.2, 0.3, 0.5, 1, 2, 3, 5, 10, 20,$ and
 217 30 mHz, calculated using the formula (1) together with Figs. 1–3 are shown in Fig. 4, and the
 218 frequency spectra $\Delta N(f_d, L)$ at $L = 2, 2.5, 3, 4, 5,$ and 6 are shown in Fig. 5. Near each curve in Fig.
 219 4, the corresponding value of f_d (mHz) is indicated, and each spectrum in Fig. 5 have the

220 corresponding L value (these values are highlighted in red). For clarity, in Figs. 4 and 5, thin
 221 curves alternate with thick curves and in Fig. 5 spectra at $L = 2$ and 2.5 are highlighted in red.



222
 223 **Figure 4.** Radial profiles $\Delta N(L, f_d)$ for protons of the ERB with drift frequencies $f_d = 0.2, 0.3, 0.5, 1, 2, 3, 5, 10, 20$ and
 224 30 mHz, plotted for periods of maximum solar activity. The f_d values corresponding to each curve are highlighted in
 225 red. For clarity, thin curves are interspersed with thick curves.



226

227

228

229

230

Figure 5. Frequency spectra $\Delta N(f_d, L)$ for protons of the ERB at $L = 2, 2.5, 3, 4, 5$ and 6 , plotted for periods of maximum solar activity. The values L corresponding to each spectrum and spectra at $L = 2$ and 2.5 are highlighted in red. The red dotted line shows the spectrum $\Delta N(f_d, L)$ of the ERB protons at $L = 2$, constructed from data during minimum periods of solar activity (see Kovtyukh, 2020). For clarity, thin curves are interspersed with thick curves.

231

232

233

The errors of these calculations consist mainly of the errors of the averaged experimental data shown in Figs. 1 and 2 (these errors are most significant at $L < 2$), and because of the deviations of the geomagnetic field from the dipole model at $L > 5$.

234

235

236

237

238

As λ_0 decreases, the errors in our calculations will decrease. These errors can be reduced also by using numerical computer calculations. However, it should be taken into account that even in very quiet periods of observations the fluxes of the ERB protons, as well as the energy spectra and pitch-angle distributions of these fluxes, may experience changes that exceed the errors of our calculations.

239

3 Discussion

240 In agreement with the results of experimental and theoretical studies, at $L > 2$, the main mechanism
241 for the formation of the ERB protons is the radial diffusion of particles from the outer boundary of
242 the geomagnetic trap to the Earth under conservation the adiabatic invariants μ and K (see, e.g.,
243 Lejosne and Kollmann, 2020; Kovtyukh, 2016b, 2018).

244 Figs. 1 and 2 presented here make it possible to determine the regions of the $\{E, L\}$ space near
245 the equatorial plane in which the ionization losses of ions during their radial diffusion can be
246 neglected and where they cannot.

247 The isolines of proton fluxes in Fig. 1 at sufficiently large E and L go up with decreasing L , in
248 the direction of increasing energy, in strict agreement with the adiabatic laws of radial transport of
249 particles. At lower L these isolines do change the direction of their course, under the influence of
250 ionization losses, which increase rapidly with decreasing L (see in Kovtyukh, 2020 for details).

251 At sufficiently large values of E and L , isolines of the anisotropy index in Fig. 2 pass practically
252 parallel to each other and parallel to the energy axis, in agreement with the laws of adiabatic
253 transport of particles with power-law energy spectra (see Kovtyukh, 1993). At lower E and L , a
254 more complex picture is formed under the influence of ionization losses (for more details see in
255 Kovtyukh, 2001, 2018).

256 With decreasing L , the radial diffusion is decreased very rapidly, and the belt of protons with E
257 > 10 – 20 MeV on $L < 2$ is generated mainly as result of decay a neutrons of albedo which are
258 knocked from the atmospheric atoms nuclei by the Galactic Cosmic Rays (GCR) protons. This
259 mechanism (CRAND) is simulated in many contemporary studies based on the experimental data
260 (see, e.g., Selesnick et al., 2007, 2013, 2014, 2018).

261 The mechanisms of formation of the ERB under the action of radial diffusion and CRAND are
262 manifested and clearly differ both in the radial profiles $\Delta N(L, f_d)$ and in the frequency spectra
263 $\Delta N(f_d, L)$ of protons.

264 Let us consider the manifestations of these mechanisms in Fig. 4 and 5 and related effects.

265 In contrast to the radial profiles of fluxes $J(L, E)$, the radial profiles $\Delta N(L, f_d)$ for protons with f_d
266 < 5 mHz (see Fig. 4) have much less steeper outer edges and their steepness decreases with
267 decreasing frequency f_d . This effect is connected mainly with an increase in the volume of
268 magnetic tubes (factor L^3 in formula (1) from Section 2.3) and with a decrease in the anisotropy
269 index of proton fluxes with increasing L .

270 At the same time, in comparison with the radial profiles $J(L, E)$, the radial profiles $\Delta N(L, f_d)$
271 have more steeper inner edges. This effect is mainly connected to the large anisotropy of proton
272 fluxes in the corresponding region of space $\{E, L\}$ and with the rapid growth of the anisotropy
273 index with decreasing L in this region. It is especially expressed in the radial profiles $\Delta N(L, f_d)$ at f_d
274 ~ 0.3 – 1 mHz (see Fig. 4); this is due to the fact that in the corresponding region of space $\{E, L\}$ the
275 anisotropy index of proton fluxes strongly depends on E and L (see Fig. 2).

276 Radial profiles $\Delta N(L, f_d)$ at $f_d > 10$ mHz are formed by the mechanism CRAND. They have a
277 maximum at $L \sim 1.5$ – 2.0 , and the steepness of their inner and outer edges does not differ as much
278 as for lower frequencies f_d (see Fig. 4). When constructing these profiles, it was taken into account
279 that at $E = 5$ – 50 MeV an anisotropy index A of proton fluxes do not depend on L at $L = 1.25$ – 1.40 :
280 $A = 12 \pm 2$ (Fischer et al., 1977; Leonov et al., 2005).

281 The shape of the spectra $\Delta N(f_d, L)$ at $L > 3$ is determined, first of all, by the shape of the energy
282 spectra of proton fluxes $J(E, L)$ at the outer boundary of the geomagnetic trap. Gradually, as the
283 particles diffuse to the Earth, their energy spectra are transformed under the action of betatron
284 acceleration and ionization losses of particles.

285 In contrast to the energy spectra of proton fluxes $J(E, L)$, distributions $\Delta N(f_d, L)$ of the ERB
286 protons over their drift frequency f_d (Fig. 5) differ much less from each other at $L > 3$. Such
287 convergence of the spectra $\Delta N(f_d, L)$ is driven by increase in the volume of magnetic tubes and a

288 decrease in the anisotropy index of the ERB proton fluxes with increasing L . Fig. 5 demonstrates
289 the closeness to the adiabatic transformations of the spectra $\Delta N(f_d, L)$ when L changes at $L > 3$.

290 The energy spectra of near-equatorial proton fluxes $J(E, L)$ with $E > 10 \cdot L^{-3}$ MeV at $L > 3$ in
291 quiet periods have a local maximum at $E = (17 \pm 3) \cdot L^{-3}$ MeV and a power-law tail ($J \propto E^{-\gamma}$, where γ
292 $= 4.25 \pm 0.75$) at $E > (36 \pm 11) \cdot L^{-3}$ MeV (Kovtyukh, 2001, 2018, 2020).

293 The frequency spectra of the ERB protons at $L > 3$ weakly depend on L and over the considered
294 range Δf_d have a close to power-law shape with an exponent $\gamma = 4.71 \pm 0.43$ (at $f_d > f_d^*$, where f_d^*
295 ~ 0.5 mHz at $L \sim 3-6$, ~ 2 mHz at $L = 2.5$ and ~ 5 mHz at $L = 2$). Note that the spread of the
296 parameter γ for the frequency spectra of protons is almost 2 times less than for their energy spectra.

297 These spectra become more rigid (flattened) at $f_d < f_d^*$.

298 Thus, the average exponents of the power-law tail of the energy and frequency spectra of
299 protons differ by $\Delta\gamma = 0.46$, and there is no local maximum in the frequency spectra at $f_d > 2$ mHz
300 at $L > 2.5$. The main role in such differences in the shape of the energy and frequency spectra of
301 protons was played by the factor $F(A)$ in formula (1), in which the anisotropy index A is a function
302 of E and L (see Figs. 2 and 3). Note that in the region $\{E > 0.5 \text{ MeV}, L > 3\}$ the anisotropy index
303 A , as well as the protons energy, is transformed according to adiabatic laws when L changes (see
304 Fig. 2 and comments to it).

305 These results confirm our hypothesis about the ordering of the distributions of protons over
306 their drift frequency f_d in the outer regions of the ERB, at $L > 3$, where most of the ERB protons
307 are located and where the radial diffusion of protons overpowers their ionization losses.

308 At all L , the frequency spectra $\Delta N(f_d, L)$ become more flat at small f_d (at small E) under
309 influence ionization losses. However, in the range of high f_d (from 3–5 mHz to 30 mHz), for
310 protons with high energies and low ionization losses, the protons frequency spectra have a power-
311 law tail even at $L = 2$ (see Fig. 5).

312 For protons with $f_d < 0.5$ mHz, which correspond to the ERB protons of the lowest energies,
313 ionization losses lead to the same consequences at higher L -shells: the radial profiles $\Delta N(L, f_d)$
314 approach each other, and the spectra $\Delta N(f_d, L)$ flatten out (see Figs. 4 and 5).

315 In the region of the steep inner edge of the radial distributions $\Delta N(L, f_d)$, spectra $\Delta N(f_d, L)$ of the
316 ERB protons become gradually increasingly rigid with decreasing L , and rapidly diverge from each
317 other (see Fig. 4 and 5). In the range of small f_d at $L < 2.5$, the connection between these
318 distributions and the shape of the boundary energy spectra of protons is gradually lost.

319 These results indicate a violation of the order in the distributions of protons under the influence
320 of ionization losses.

321 In Fig. 5, the dotted line also shows the spectrum $\Delta N(f_d, L)$ of the ERB protons at $L = 2$,
322 constructed from experimental data for periods of low solar activity between the 19th/20th,
323 20th/21th, 21th/22th, and 22th/23th solar cycles (see Fig. 1 in Kovtyukh, 2020). Fig. 5 show that at
324 $L = 2$ for $f_d > 10$ mHz there were more protons at the minimum of solar activity, and for $f_d \sim 1-10$
325 mHz there were more protons at the maximum of solar activity.

326 The effect of a decrease in the $\Delta N(f_d, L)$ values for protons with $f_d > 10$ mHz at $L < 2$ with an
327 increase in solar activity is mainly connected with a decrease in the fluxes of protons with $E > 10-$
328 20 MeV here. This effect is well known. It is described by the CRAND mechanism (see, e.g.,
329 Selesnick et al., 2007) and was considered in detail in (Kovtyukh, 2020). With an increase in solar
330 activity, the densities of atmospheric atoms and ionospheric plasma on small L -shells significantly
331 increase, which leads to an increase in ionization losses of the ERB protons, and the power of their
332 main source (CRAND) practically does not change. As a result, the equilibrium fluxes and $\Delta N(f_d,$
333 $L)$ for protons with $f_d > 10$ mHz are established at lower levels.

334 However, the effect of an increase in $\Delta N(f_d, L)$ for $f_d \sim 1\text{--}10$ mHz at low L with increasing solar
335 activity, corresponding to the protons of lower energies, was discovered here for the first time.

336 With decreasing E (and f_d) of protons their ionization losses increase, and if the fluxes of
337 low-energy protons in the inner belt were also formed by the CRAND mechanism, one would have
338 observed even stronger increase of their fluxes with decreasing solar activity, than for protons with
339 $E > 10\text{--}20$ MeV ($f_d > 10$ mHz). But for protons with $f_d \sim 1\text{--}10$ mHz, we see in Fig. 5 the opposite
340 effect in the spectra $\Delta N(f_d, L)$ at $L = 2$, which is not described by the CRAND mechanism.

341 On the other hand, it was proved that quasi-stationary fluxes of protons with $E < 15$ MeV at $L \sim$
342 2 are formed mainly by the mechanism of protons radial diffusion from the external region of the
343 ERB (Selesnick et al., 2007, 2013, 2014, 2018). These fluxes and $\Delta N(f_d, L)$ values for $f_d \sim 1\text{--}10$
344 mHz at $L = 2$ are formed as a result of a balance of competing processes radial diffusion of protons
345 and their ionization losses.

346 The rates of transport of the ERB protons to the Earth (radial diffusion) rapidly increase with
347 decreasing particles energy (see Kovtyukh, 2016b). In addition, with an increase in solar activity,
348 the average level of geomagnetic fluctuations in the ERB increases. Under the influence of these
349 factors, one can expect a significant increase in the intensity of radial diffusion of the low-energy
350 protons at low L with an increase in solar activity. As a result, the effect of increasing in the
351 density of a dissipative medium with an increase in solar activity is overpowered by a more
352 significant effect of increasing in the rates of radial diffusion of protons.

353 According to numerous experimental data, during magnetic storms, a wide variety of complex
354 spectra of powerful pulsations of magnetic and electric fields in the considered frequency range
355 (ULF) can be generate in the geomagnetic trap, which are non-regularly distributed over L ; these
356 pulsations can lead to local acceleration and losses of the ERB particles (see, e.g., Sauvaud et al.,
357 2013). Such effects will violate the regular characteristics of the protons distributions shown in
358 Fig. 4 and 5. However, during quiet periods ($K_p < 2$), the amplitudes of such pulsations are small
359 and they lead only to radial diffusion of particles.

360 4 Conclusions

361 From the data on near-equatorial ERB proton fluxes (with energy from 0.2 to 100 MeV and drift L
362 shells ranging from 1 to 8), their quasi-stationary distributions over the drift frequency of particles
363 around the Earth (f_d) were constructed. The results of calculations of the number ΔN of the ERB
364 protons within 30° in geomagnetic latitude at different L and f_d for periods of maximum solar
365 activity are presented. They differ from the corresponding distributions of the ERB protons for
366 periods of low solar activity only at $L < 2.5$ (for comparison, the spectra of these distributions are
367 given at $L = 2$).

368 The radial profiles of these distributions $\Delta N(L, f_d)$ have only one maximum that shifts toward
369 the Earth with increasing f_d . In comparison to the proton fluxes profiles $J(L, E)$, the radial profiles
370 $\Delta N(L, f_d)$ at $f_d < 5$ mHz have steeper inner edges and flatter outer edges. However, the radial
371 profiles $\Delta N(L, f_d)$ at $f_d > 10$ mHz, which are formed by the CRAND mechanism, have inner and
372 outer edges with only slightly difference from each other for what concerns the steepness of their
373 profiles.

374 In contrast to the energy spectra of proton fluxes $J(E, L)$, the frequency spectra $\Delta N(f_d, L)$ of the
375 ERB protons at $L > 3$ are weakly dependent on L and, for sufficiently large f_d they have a nearly
376 power-law shape with an exponent $\gamma = 4.71 \pm 0.43$. There is no local maximum in these spectra in
377 the region $\{f_d > 2 \text{ mHz}, L > 2.5\}$, as in the corresponding $J(E, L)$ spectra.

378 The main physical processes in the ERB (radial diffusion, ionization losses of particles and
379 mechanism CRAND) manifested clearly in these distributions.

380 Distributions $\Delta N(L, f_d)$ and $\Delta N(f_d, L)$ of the ERB protons in the region $\{f_d > 0.5 \text{ mHz}, L > 3\}$
381 have a more regular shape than in the corresponding region of the space $\{E, L\}$. In these regions,
382 there is the majority of the ERB protons, and their radial diffusion overpowers their ionization
383 losses during the transport of particles to the Earth.

384 In the region of the steep inner edges of the radial distributions $\Delta N(L, f_d)$, the spectra $\Delta N(f_d, L)$
385 of protons rapidly diverge from each other with decreasing L , and at low frequencies these spectra
386 become flatten. These results indicate a violation of the order in these distributions of protons
387 under the influence of ionization losses.

388 With increasing solar activity, the number of protons $\Delta N(f_d, L)$ at $L \sim 2$ decreases for $f_d > 10$
389 mHz and increases for $f_d \sim 1\text{--}10$ mHz. The effect at high f_d , corresponding to protons with $E > 15$
390 MeV, is well known and is described in the framework of the CRAND mechanism.

391 However, the opposite effect at low f_d , corresponding to the lower-energy protons, is discovered
392 here for the first time. This effect can be associated with the fact that the low-frequency part of the
393 spectrum $\Delta N(f_d, L)$ of protons, even at $L \sim 2$, is mainly formed by the mechanism of protons
394 transport from the outer regions of the ERB. This effect may indicate that with increasing solar
395 activity, the average rates of radial diffusion of protons increase as well. For low-energy protons at
396 $L \sim 2$, the effect of increasing density of a dissipative medium with increasing solar activity is
397 overpowered by the increase of the rates of radial diffusion of particles.

398 Comparing this result with the results for ions with $Z \geq 2$ at $L > 2.5$ (see Kovtyukh, 2020), one
399 can conclude that the amplitude of solar-cyclic variations of the radial diffusion coefficient D_{LL}
400 increases with decreasing E and L (Z is the charge of the atomic nucleus with respect to the charge
401 of the proton).

402

403 *Data availability.* All data from this investigation are presented in Figs. 1–5.

404 *Competing interests.* The author declares that there is no conflict of interest.

405 *Acknowledgements.* The author is very grateful to the reviewers for their important and fruitful
406 comments and proposals regarding the paper and to topical editor, Dr. Elias Roussos, for editing
407 this paper.

408 *Review statement.* This paper was edited by Elias Roussos and reviewed by two anonymous
409 referees.

410

411

412 **References**

- 413 Alfvén, H., and Fälthammar, C.-G.: *Cosmical Electrodynamics, Fundamental Principles*,
414 Clarendon Press, Oxford, 1963.
- 415 Davis, L. R.: Low energy trapped protons and electrons, *Proc. Plasma Space Sci. Symp.*, Eds. D.
416 B. Chang and C. Y. Huang, Washington, P. 212–226, 1965.
- 417 Fennell, J. F., Blake, J. B., and Paulikas, G. A.: Geomagnetically trapped alpha particles, 3. Low-
418 altitude outer zone alpha-proton comparisons, *J. Geophys. Res.*, **79**(4), 521–528,
419 <https://doi.org/10.1029/JA079i004p00521>, 1974.
- 420 Fischer, H. M., Auschrat, V. W., and Wibberenz, G.: Angular distribution and energy spectra of
421 protons of energy $5 \leq E \leq 50$ MeV in the lower edge of the radiation belt in equatorial latitudes,
422 *J. Geophys. Res.*, **82**(4), 537–547, <https://doi.org/10.1029/JA082i004p00537>, 1977.
- 423 Fritz, T. A., and Spjeldvik, W. N.: Steady-state observations of geomagnetically trapped energetic
424 heavy ions and their implications for theory, *Planet. Space Sci.*, **29**(11), 1169–1193,
425 [https://doi.org/10.1016/0032-0633\(81\)90123-9](https://doi.org/10.1016/0032-0633(81)90123-9), 1981.
- 426 Garcia, H. A., and Spjeldvik, W. N.: Anisotropy characteristics of geomagnetically trapped ions, *J.*
427 *Geophys. Res.*, **90**(A1), 359–369, <https://doi.org/10.1029/JA090iA01p00359>, 1985.
- 428 Hoffman, R. A., and Bracken, P. A.: Magnetic effects of the quiet-time proton belt, *J. Geophys.*
429 *Res.*, **70**(15), 3541–3556, <https://doi.org/10.1029/JZ070i015p03541>, 1965.
- 430 Ilyin, B. D., Kuznetsov, S. N., Panasyuk, M. I., and Sosnovets, E. N.: Non-adiabatic effects and
431 boundary of the trapped protons in the Earth's radiation belts, *Bulletin of the Russian Academy*
432 *of Sciences: Physics*, **48**(11), 2200–2203, 1984.
- 433 Kovtyukh, A. S.: Relation between the pitch-angle and energy distributions of ions in the Earth's
434 radiation belts, *Geomagn. Aeron.*, **33**(4), 453–460, 1993.
- 435 Kovtyukh, A. S.: Geocorona of hot plasma, *Cosmic Res.*, **39**(6), 527–558,
436 <https://doi.org/10.1023/A:1013074126604>, 2001.
- 437 Kovtyukh, A. S.: Radial dependence of ionization losses of protons of the Earth's radiation belts,
438 *Ann. Geophys.*, **34**(1), 17–28, <https://doi.org/10.5194/angeo-34-17-2016>, 2016a.
- 439 Kovtyukh, A. S.: Deduction of the rates of radial diffusion of protons from the structure of the
440 Earth's radiation belts, *Ann. Geophys.*, **34**(11), 1085–1098, [https://doi.org/10.5194/angeo-34-](https://doi.org/10.5194/angeo-34-1085-2016)
441 [1085-2016](https://doi.org/10.5194/angeo-34-1085-2016), 2016b.
- 442 Kovtyukh, A. S.: Ion Composition of the Earth's Radiation Belts in the Range from 100 keV to
443 100 MeV/nucleon: Fifty Years of Research, *Space Sci. Rev.*, **214**(8), 124:1–124:30,
444 <https://doi.org/10.1007/s11214-018-0560-z>, 2018.
- 445 Kovtyukh, A. S.: Earth's radiation belts' ions: patterns of the spatial-energy structure and its solar-
446 cyclic variations, *Ann. Geophys.*, **38**(1), 137–147, doi:10.5194/angeo-38-137-2020, 2020.
- 447 Lejosne, S., and Kollmann, P.: Radiation Belt Radial Diffusion at Earth and Beyond, *Space Sci.*
448 *Rev.*, **216**(1), 19:1–19:78, <https://doi.org/10.1007/s11214-020-0642-6>, 2020.
- 449 Leonov, A., Cyamukungu, M., Cabrera, J., Leleux, P., Lemaire, J., Gregorie, G., Benck, S.,
450 Mikhailov, V., Bakaldin, A., Galper, A., Koldashov, S., Voronov, S., Casolino, M., De Pascale,
451 M., Picozza, P., Sparvulli, R., Ricci, M.: Pitch-angle distribution of trapped energetic protons
452 and helium isotop nuclei measured along the Resurs-01 No.4 LEO satellite, *Ann. Geophys.*,
453 **23**(8), 2983–2987, <https://doi.org/10.5194/angeo-23-2983-2005>, 2005.
- 454 Northrop, T. G.: *The Adiabatic Motion of Charged Particles*, Wiley-Interscience, NY, USA, 1963.
- 455 Parker, E. N.: Newtonian development of the dynamical properties of ionized gases of low density,
456 *Phys. Rev.*, **107**(4), 924–933. <https://doi.org/10.1103/PhysRev.107.924>, 1957.
- 457 Roederer, J. G.: *Dynamics of Geomagnetically Trapped Radiation*, Springer, NY, USA, 1970.
- 458 Sauvaud, J.-A., Walt, M., Delcourt, D., Benoist, C., Penou, E., Chen, Y., and Russell C. T.: Inner
459 radiation belt particle acceleration and energy structuring by drift resonance with ULF waves

460 during geomagnetic storms, *J. Geophys. Res. Space Physics*, **118**(4), 1723–1736,
461 <https://doi.org/10.1002/jgra.50125>, 2013.

462 Selesnick, R. S., Looper, M. D., and Mewaldt, R. A.: A theoretical model of the inner proton
463 radiation belt, *Space Weather*, **5**(4), S04003, <https://doi.org/10.1029/2006SW000275>, 2007.

464 Selesnick, R. S., Hudson, M. K., and Kress B. T.: Direct observation of the CRAND proton
465 radiation belt source, *J. Geophys. Res. Space Phys.*, **118**(12), 7532–7537,
466 <https://doi.org/10.1002/2013JA019338>, 2013.

467 Selesnick, R. S., Baker, D. N., Jaynes, A. N., Li, X., Kanekal, S. G., Hudson, M. K., and Kress, B.
468 T.: Observations of the inner radiation belt: CRAND and trapped solar protons, *J. Geophys.
469 Res. Space Phys.*, **119**(8), 6541–6552, <https://doi.org/10.1002/2014JA020188>, 2014.

470 Selesnick, R. S., Baker, D. N., Kanekal, S. G., Hoxie, V. C., and Li, X.: Modeling the proton
471 radiation belt with Van Allen Probes Relativistic Electron-Proton Telescope data, *J. Geophys.
472 Res. Space Phys.*, **123**(1), 685–697, <https://doi.org/10.1002/2017JA024661>, 2018.

473 Shi, R., Summers, D., Ni, B., Manweiler, J. W., Mitchell, D. G., and Lanzerotti, L. J.: A statistical
474 study of proton pitch-angle distributions measured by the Radiation Belt Storm Probes Ion
475 Composition Experiment, *J. Geophys. Res. Space Phys.*, **121**(6), 5233–5249,
476 <https://doi.org/10.1002/2015JA022140>, 2016.

477 Shi, R., Summers, D., Ni, B., Manweiler, J. W., Mitchell, D. G., and Lanzerotti, L. J.: A statistical
478 study of proton pitch-angle distributions measured by the Radiation Belt Storm Probes Ion
479 Composition Experiment, *J. Geophys. Res. Space Phys.*, **121**(6), 5233–5249,
480 <https://doi.org/10.1002/2015JA022140>, 2016.

481 Søråas, F., and Davis, L.R.: Temporal variations of 100 keV to 1700 keV trapped protons observed
482 on satellite Explorer 26 during first half of 1965, Rep. X-612-68-328, NASA Goddard Space
483 Flight Cent., Greenbelt, Md., 1968.

484 Williams, D. J., and Lyons, L. R.: The proton ring current and its interaction with plasmopause:
485 Storm recovery phase, *J. Geophys. Res.*, **79**(28), 4195–4207,
486 <https://doi.org/10.1029/JA079i028p04195>, 1974.

487 Williams, D. J., and Frank, L. A.: Intense low-energy ion populations at low equatorial altitude, *J.
488 Geophys. Res.*, **89**(A6), 3903–3911, <https://doi.org/10.1029/JA089iA06p03903>, 1984.